

HI Galaxy Signatures in the SRAO MeerKAT Galactic Plane Survey – II. The Local Void and its substructure

Sushma Kurapati^{1*}, Renée C. Kraan-Korteweg¹, D.J. Pisano¹, Hao Chen^{1,2}, Sambatriniaina H. A. Rajohnson¹, Nadia Steyn^{1,3}, Bradley Frank^{4,5,6,1}, Paolo Serra⁷, Sharmila Goedhart⁵, Fernando Camilo⁵

¹ Department of Astronomy, University of Cape Town, Private Bag X3, Rondebosch 7701, South Africa

² Research Center for Intelligent Computing Platforms, Zhejiang Laboratory, Hangzhou 311100, China

³ International Centre for Radio Astronomy Research (ICRAR), The University of Western Australia, 35 Stirling Highway, Australia

⁴ UK Astronomy Technology Centre, Royal Observatory Edinburgh, Blackford Hill, Edinburgh EH9 3HJ, UK

⁵ South African Radio Astronomy Observatory, 2 Fir Street, Observatory, 7925, South Africa

⁶ The Inter-University Institute for Data Intensive Astronomy (IDIA), and University of Cape Town, Private Bag X3, Rondebosch, 7701, South Africa

⁷ INAF – Osservatorio Astronomico di Cagliari, Via della Scienza 5, 09047, Selargius, CA, Italy

Accepted XXX. Received YYY; in original form ZZZ

ABSTRACT

The Local Void is one of the nearest large voids, located at a distance of 23 Mpc. It lies largely behind the Galactic Bulge and is therefore extremely difficult to observe. We use HI 21 cm emission observations from the SRAO MeerKAT Galactic Plane Survey (SMGPS) to study the Local Void and its surroundings over the Galactic longitude range $329^\circ < \ell < 55^\circ$, Galactic latitude $|b| < 1.5^\circ$, and redshift $cz < 7500 \text{ km s}^{-1}$. We have detected 291 galaxies to median rms sensitivity of 0.44 mJy per beam per 44 km s^{-1} channel. We find 17 galaxies deep inside the Void, 96 at the border of the Void, while the remaining 178 galaxies are in average density environments. The extent of the Void is ~ 58 Mpc. It is severely under-dense for the longitude range $350^\circ < \ell < 35^\circ$ up to redshift $z < 4500 \text{ km s}^{-1}$. The galaxies in the Void tend to have HI masses that are lower (by approximately 0.25 dex) than their average density counterparts. We find several potential candidates for small groups of galaxies, of which two groups (with 3 members and 5 members) in the Void show signs of filamentary substructure within the Void.

Key words: galaxies: evolution - galaxies: ISM - galaxies: HI surveys – radio interferometry: MeerKAT – cosmology: large-scale structure of Universe – radio lines: galaxies

1 INTRODUCTION

Galaxies are distributed in a ‘cosmic web’ consisting of voids, interconnected filaments, walls, and nodes surrounding vast low-density regions (e.g. Jones et al. 2009; Tempel et al. 2014). Voids form prominent features of this ‘cosmic web’ (van de Weygaert & Platen 2011). They are extended regions with sizes in the range of 20 – 50 h^{-1} Mpc that are largely devoid of galaxies and occupy a major fraction of the volume of the universe. The voids provide a unique opportunity to study galaxies at an earlier stage of their evolution because galaxies in voids typically evolve at later times than those in the dense regions (e.g. Aragon-Calvo & Szalay 2013). For example, extremely low metallicity dwarf galaxies have been found in voids, suggestive of a slow evolution (e.g. Pustilnik

et al. 2006; Pustilnik & Tepliakova 2011). The void galaxies are also largely unaffected by complex environmental processes that modify galaxies in higher density environments and thereby retain important clues regarding their formation and evolution. The voids are expected to have substructure consisting of sub-voids, tendrils, filaments, walls, and nodes because the structure formation in voids is similar to structure formation in a low density universe (Goldberg & Vogeley 2004; Aragon-Calvo & Szalay 2013; Alpaslan et al. 2014). Numerical simulations suggest that the galaxies in voids may preferentially lie within these filamentary void substructures (Sheth & van de Weygaert 2004; van de Weygaert & Platen 2011; Aragon-Calvo & Szalay 2013; Rieder et al. 2013). Hence, it is interesting to explore whether the intricate substructure expected from hierarchical structure formation processes can be traced observationally.

Observations of void galaxies have shown that they are

* E-mail: sushma@ast.uct.ac.za

statistically bluer, fainter, hence of later morphological type, and have higher specific star formation rates compared to their counterparts in average density environments (Rojas et al. 2004, 2005; Hoyle et al. 2005; Blanton et al. 2005; Croton et al. 2005; Park et al. 2007; Croton & Farrar 2008; Hoyle et al. 2012; Ricciardelli et al. 2014; Moorman et al. 2014, 2015). However, controversy persists in the literature as to whether the void galaxies have different intrinsic properties compared to similar galaxies in average density regions (e.g. Patiri et al. 2006; Park et al. 2007; von Benda-Beckmann & Müller 2008; Kreckel et al. 2012; Moorman et al. 2016; Kurapati et al. 2018, 2020; Jian et al. 2022). Voids contain a population of galaxies that are relatively gas rich, many of which present evidence for ongoing gas accretion, interactions with small companions and filamentary alignments (e.g. Ekta et al. 2008; Kreckel et al. 2011, 2012; Beygu et al. 2013; Chengalur & Pustilnik 2013; Chengalur et al. 2017; Kurapati 2020). Numerical simulations predict that low density regions at $z \sim 0$ are dominated by cold gas accretion (e.g. Kereš et al. 2005, 2009; Dekel et al. 2013). For example, Stanonik et al. (2009) found an extremely extended and massive HI polar disk galaxy providing a convincing case for cold mode accretion. Voids are therefore uniquely promising places to search for evidence of ongoing gas accretion.

At a distance of ~ 23 Mpc (Tully 1987; Tully et al. 2008), the ‘Local Void’ (LV) is the nearest void in the local universe. Studies of cosmic flows in the Local Volume have demonstrated motions of galaxies away from the LV (e.g. Tully et al. 2008; Karachentsev et al. 2015; Rizzi et al. 2017; Shaya et al. 2017; Anand et al. 2018; Tully et al. 2019). Studying the size, census, and emptiness of the LV is critical to understand the distribution of mass responsible for the motion of galaxies. In addition, the proximity of the LV allows us to study its galaxies in detail down to very faint dwarf galaxies.

However, the LV has been difficult to study since a major fraction lies behind the Galactic Bulge of our own Milky Way. The high foreground extinction and the high stellar density mask galaxies at optical/infrared wavelengths, which impacts a thorough study of the LV despite its proximity. HI 21-cm line observations is one of the few methods that allows an investigation of its galaxy population through the thickest Galactic obscuration. The Parkes single dish multi-beam HI surveys such as HIPASS (Meyer et al. 2004; Wong et al. 2006) and HIZOA (Donley et al. 2005; Kraan-Korteweg et al. 2008; Staveley-Smith et al. 2016, Kraan-Korteweg et al. in prep) confirmed the LV to be severely underdense. While these shallow surveys uncovered some galaxies in the Local Void, we still do not have a good census of the Void though.

We therefore decided to make use of the data that was taken as part of the SARAo MeerKAT Galactic Plane Survey (SMGPS; Goedhart et al., in prep). The sensitivity and depth of the SMGPS provides us with a valuable data set to learn more about the void population. In this paper, we present SMGPS HI observations of the LV and its surroundings in the Zone of Avoidance (ZOA) over the Galactic longitude range $329^\circ < \ell < 55^\circ$, Galactic latitude $|b| < 1.5^\circ$, and redshift $z < 7500 \text{ km s}^{-1}$, which is henceforth referred to as the LV-SMGPS survey. This is the largest blind wide-area interferometric HI survey of void galaxies. Weinberg et al. (1991) conducted the first blind interferometric HI survey

in a void situated in the foreground of the Perseus-Pisces supercluster. However, no galaxies were detected in the void during their survey. Other previous high-resolution studies on void galaxies were based on targeted observations around the optically selected galaxies, and hence, are biased by the selection criterion (e.g. Szomoru et al. 1996; Kreckel et al. 2012; Kurapati 2020).

2 MEERKAT OBSERVATIONS & DATA REDUCTION

2.1 The SARAo MeerKAT Galactic Plane Survey

SMGPS survey is a systematic HI survey that covers $248^\circ < \ell < 60^\circ$ and $|b| < 1.5^\circ$. The survey didn’t include the Galactic centre region, $358^\circ < \ell < 2^\circ$ which was covered by Heywood et al. (2022). The main scientific goals of the SMGPS are the studies of the Galaxy itself and its objects. However, we can extract the 21 cm spectral line observations to explore the large scale structure through their HI emission and trace hidden structures such as the Great Attractor (GA), the Vela supercluster (VSCL), and the Local Void (LV), the primary focus here. This paper is the second in a series leveraging HI data from the SMGPS survey. The first paper explores the Great Attractor (Steyn et al. 2023, under review in MNRAS), while the third paper is on the Vela supercluster (Rajonson et al. in prep), which together improve our understanding of the dynamics in the local universe.

2.2 Data reduction

The observations were carried out with the full MeerKAT array in the L-band (856–1712 MHz) using the MeerKAT SKARAB 4k-correlator, which gives a frequency resolution of ~ 209 kHz that corresponds to a rest frame velocity resolution $\sim 44.1 \text{ km s}^{-1}$ at $z = 0$. Each MeerKAT pointing has an effective integration of ~ 1 hour, but the observations were done in small sub-integrations spread over ~ 10 hours to retain excellent u-v coverage.

The LV-SMGPS raw data were downloaded from the SARAo Archive for the range 1308–1430 MHz enabling us to detect galaxies out to $\sim 25,000 \text{ km s}^{-1}$. We use the Containerised Automated Radio Astronomy Calibration (CARACal) pipeline (Józsa et al. 2020) to reduce the raw data. CARACal is based on STIMELA, a radio interferometry scripting framework based on container technologies and Python (Makhathini 2018). It uses many publicly available radio interferometry software packages such as CASA, Cubical, WSClean and Montage, etc. The pipeline carried out all the standard data reduction tasks including flagging, cross-calibration, self-calibration, continuum subtraction, and spectral line imaging. We perform the standard cross-calibration procedures such as delay, bandpass and gain calibrations, and later use the self-calibration of the continuum to further improve the quality of the calibration. We use Cubical (Kenyon et al. 2018) to carry out two rounds of self calibration. Further, the continuum sky model that was generated after self-calibration is subtracted from the visibilities.

For the HI imaging of the individual fields, we use WSClean with robust=0 weighting and a taper of $15''$. This

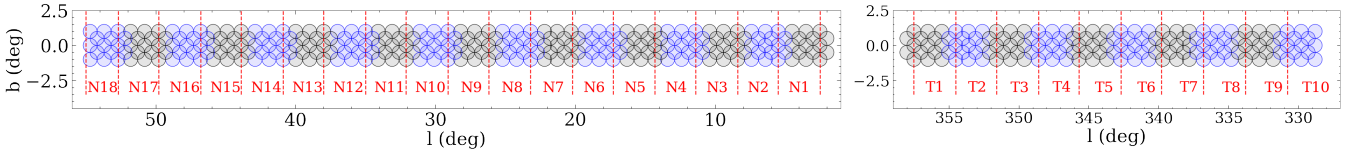


Figure 1. Mosaic configuration of the LV-SMGPS of 28 mosaics of 22 fields each with Galactic longitude, $2^\circ < \ell < 55^\circ$ (left: N1- N18) and $329^\circ < \ell < 359^\circ$ (right: T1-T10) and $-1.5^\circ < b < 1.5^\circ$. Each circle represents a MeerKAT pointing and our region of interest corresponds to a total of 440 MeerKAT pointings.

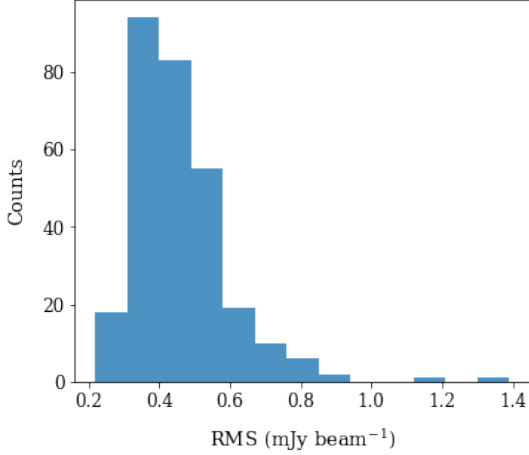


Figure 2. Histogram of RMS noise measured around each detection. The median RMS noise is $0.42 \text{ mJy beam}^{-1}$ per 44.1 km s^{-1} channel.

gives us dirty HI cubes with a nearly Gaussian beam size of $30'' \times 27'' (\pm 2'')$, which is sufficient for our science goals. The HI data cubes were also made at lower resolutions using taper $30''$ and taper $60''$ to obtain maps with beam sizes closer to FWHM $45''$ and $67''$, ensuring that we do not miss out on nearby very extended low column density sources. A more detailed description of the data reduction strategy and data quality assessment is presented in Rajohnson et al., in prep.

In this paper, we present the data for the region in and around the Galactic Bulge, $329^\circ < \ell < 358^\circ$ and $2^\circ < \ell < 55^\circ$ and $-1.5^\circ < b < 1.5^\circ$, which corresponds to a total of 440 MeerKAT64 pointings. Individual data cubes were primary-beam corrected and are stitched together to create mosaic cubes to maximize the sensitivity as shown in Fig. 1. We use the CARACAL pipeline to construct 28 HI mosaic cubes, each mosaic cube consisting of 22 contiguous primary-beam corrected HI data cubes of partly overlapping pointings, covering an area of $4^\circ \times 3^\circ$. The mosaics were offset by $\Delta\ell = 3^\circ$ to detect extended sources on the borders of mosaics and to allow for independent assessment of the quality of the data products in the overlapping regions.

2.3 HI detections

We use the Source Finding Application SoFiA pipeline (Serra et al. 2015; Westmeier et al. 2021) which is designed for automatic HI source finding in interferometric spectral line data. SoFiA2 (<https://github.com/SoFiA-Admin/SoFiA-2>) is applied to detect HI sources in the redshift range

$300 \text{ km s}^{-1} < V_{\text{hel}} < 7500 \text{ km s}^{-1}$ which covers the full depth of the LV with its borders but excludes the channels containing Milky Way emission. We do not consider the edges of the mosaic images, where sensitivity is reduced, and the SoFiA search area is limited to $3.5^\circ \times 3^\circ$ with a remaining overlap of 0.25° on each side of the mosaic. Within SoFiA, we remove noise variations in the mosaic cubes by using the noise images that were obtained as part of mosaicking algorithm. We use the ‘smooth+clip’ algorithm which smooths the cube spatially and spectrally with multiple user-defined Gaussian and boxcar kernels respectively. We apply a threshold of 5σ using 4 Gaussian smoothing kernels that resulted in angular resolutions of no smoothing, $30''$, $60''$, and $90''$, in addition to three spectral boxcar kernels of no smoothing, 133 , and 308 km s^{-1} . We merge the detected voxels into individual sources by using a merging radius of a beam along both the RA and Dec axes, and 2 channels (with channel width $\sim 44.1 \text{ km s}^{-1}$) in velocity.

Each of the SoFiA runs yields a list of real and false positive detections. It is not possible to assess the reliability of sources by searching for a plausible optical counterpart within the SoFiA-2 mask since we do not have any multi-wavelength data this close to the Galactic plane. We therefore inspect the channel maps, moment maps, and spectra of all possible detections obtained using SoFiA to assess the reliability of galaxy candidates. We derive the moment maps of all the possible detections by smoothing the cubelets centred on each detection to a circular beam of $35'' \times 35''$ and clipping it at 3σ threshold, where σ is the average RMS noise around each detection (e.g. Ponomareva et al. 2021). Moment maps were then derived by applying the resulting mask to the original resolution unsmoothed cubelet to account for a low column density diffuse HI emission. This mask was also used to derive the spectrum from the unsmoothed cube for each source. Further, we check for velocity continuity of HI emission, expected HI size for a given HI mass, significance of HI emission in the spectrum, etc to classify each source as either a definite detection or a false detection. This leads to a total of 291 definite detections.

To determine the RMS noise levels around each detection, we take the average RMS from four emission-free regions around the detection. The histogram of the RMS noise is shown in Fig. 2. The RMS noise per channel varies from 0.22 to $1.32 \text{ mJy beam}^{-1}$ with a median noise level of $\text{RMS} = 0.42 \text{ mJy beam}^{-1}$. We show masked moment-0 (left panel), masked moment-1 map (middle panel), and the global HI profile (right panel) of some of the definite detections in Figure A1 in Appendix. The moment maps and spectra for all the detections are available online. The galaxy ID (Jhh-mmss \pm ddmss) for each galaxy is shown on the top-left of moment 0 map. The synthesis beam FWHM is indicated by

Table 1. An extract of the LV-SMGPS catalogue listing HI parameters of galaxies. This table is published in its entirety online in the machine readable format

Name SMGPS-HI- (1)	Mosaic (2)	ℓ deg (3)	b deg (4)	S_{int} Jy km s ⁻¹ (5)	$\sigma_{S_{\text{int}}}$ Jy km s ⁻¹ (6)	S_{peak} Jy (7)	RMS mJy beam ⁻¹ (8)	V_{hel} km s ⁻¹ (9)	w_{50} km s ⁻¹ (10)	w_{20} km s ⁻¹ (11)	$\log(M_{\text{HI}})$ $\log(M_{\odot})$ (12)	Flag (13)	Note (14)
J175227-262618	N01	2.92	-0.01	0.39	0.21	0.007	0.46	6024	204	96	8.85	1	
J175200-260838	N01	3.12	0.23	2.62	0.33	0.010	0.59	7115	326	280	9.82	1	
J175024-254605	N01	3.26	0.73	2.04	0.27	0.018	0.54	6162	217	188	9.59	1	
J174806-252644	N01	3.27	1.34	1.04	0.38	0.013	0.71	6024	139	139	9.28	1	
J175321-254318	N01	3.64	0.18	1.75	0.25	0.026	0.54	6284	107	60	9.54	1	
J175537-254553	N01	3.86	-0.28	3.24	0.37	0.020	0.68	7134	414	381	9.92	1	
J175725-253712	N01	4.19	-0.56	1.13	0.18	0.010	0.49	5886	195	132	9.29	1	
J175857-252902	N01	4.48	-0.79	5.46	0.88	0.030	0.56	6886	276	260	10.11	1	
J175618-250448	N01	4.53	-0.07	4.23	0.92	0.022	0.68	7682	354	312	10.10	1	
J175258-242216	N01	4.76	0.94	4.76	0.20	0.022	0.55	6459	266	224	10.00	1	
J175320-241850	N01	4.85	0.90	2.30	0.12	0.018	0.45	6477	186	163	9.68	1	
J175325-241645	N01	4.89	0.90	1.81	0.12	0.014	0.48	6508	163	139	9.58	1	
J175330-241811	N01	4.88	0.87	1.46	0.23	0.010	0.45	6325	186	139	9.46	1	

an ellipse in both the moment 0 and moment 1 maps. The HI global profile is shown by solid black line, the smoothed profile by a black dashed line, the solid red line indicates the heliocentric velocity.

We calculate the integrated flux from the SoFiA output as well as the spectrum. The fluxes measured with the two methods agree within $\sim 10\%$. To calculate the error of the integrated flux, we project the 3D source mask on to eight emission free regions (four regions at $v_{\text{sys}} - 220$ km s⁻¹ and other four at $v_{\text{sys}} + 220$ km s⁻¹) surrounding the detection in voxels and measure the signal in each of the 8 projected masks. The uncertainty in the integrated flux is then defined as the RMS scatter from the flux measurements in the eight projected masks (e.g. Ramatsoku et al. 2016; Ponomareva et al. 2021). Further, we calculate the HI mass using the standard formula, $M_{\text{HI}} = 2.356 \times 10^5 D^2 S_{\text{int}} M_{\odot}$, where D is the distance in Mpc, S_{int} is the integrated flux density in Jy km s⁻¹. The HI redshift was extracted from the SoFiA output and the luminosity distance was calculated for each source based on its HI redshift and assuming the cosmological values of $\Omega_M = 0.3$, $\Omega_{\Lambda} = 0.7$, and $H_0 = 70$ km s⁻¹ Mpc⁻¹ from the standard Λ CDM cosmology.

2.3.1 LV-SMGPS Catalogue

An extract of the LV-SMGPS catalogue listing the HI parameters for the detected galaxies is shown in Table 1. The full catalogue is given in table ?? in the Appendix.

The columns are as follows:

Column 1 - Name of the galaxy: The format (SMGPS-HI) JHHMMSS-DDMMSS represents the rounded values of RA and Declination

Column 2 - Mosaic (Txx or Nxx from Fig. 1) in which the galaxy is detected

Column 3 and 4 - Galactic coordinates, ℓ and b in deg

Column 5 and 6 - Integrated flux, S_{int} along with its corresponding error $\sigma_{S_{\text{int}}}$ in Jy km s⁻¹

Column 7 - Peak flux, S_{peak} in Jy

Column 8 - Measured local RMS around the detection in mJy beam⁻¹ per 44.1 km s⁻¹ channel

Column 9 - Optical heliocentric velocity, V_{hel} in km s⁻¹

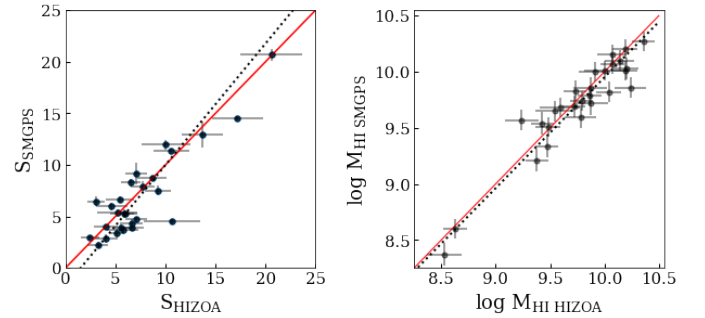


Figure 3. Comparison of integrated flux in Jy km s⁻¹ (left panel) and HI Mass in $\log(M_{\odot})$ (right panel) between LV-SMGPS and HIZOA. The red solid line represents $x=y$ line and the black dotted line represents the linear regression.

Column 10 and 11 - Line widths w_{50} and w_{20} in km s⁻¹. These values represent the measured linewidths at 50% and 20% of the peak flux, respectively

Column 12 - Logarithm of the HI mass, $\log M_{\text{HI}}$ in $\log(M_{\odot})$

Column 13 - Flag (category 1 indicates a definite detection and category 2 indicates a possible detection)

Column 14 - Notes on galaxies. It describes whether a galaxy is interacting, has a companion, or any other relevant information.

2.3.2 HI data assessment

We verified the measured HI fluxes and HI masses by comparing them to the detections from the Parkes HI Zone of Avoidance (HIZOA) survey (Staveley-Smith et al. 2016) and the Northern Extension of HIZOA survey (Donley et al. 2005). The HIZOA survey is a ‘blind’ wide area systematic HI survey of the southern Zone of Avoidance using the Parkes single dish telescope equipped with the multi-beam receiver ($|b| < 5^{\circ}$, RMS ~ 6 mJy beam⁻¹). There are 32 galaxies in this region that have HIZOA counterparts. All HIZOA galaxies are recovered in our analysis. Five of the galaxies were found to be resolved into two or more galaxies by the LV-SMGPS observations: HIZOA J1753-24A is

Table 2. Comparison of HIZOA and LV-SMGPS parameters for the HIZOA sources

HIZOA ID	SMGPS ID	ℓ	b	V_{hel}	$S_{\text{int,HIZOA}}$	$S_{\text{int,SMGPS}}$	$\log M_{\text{HI}}$	$\log M_{\text{HI}}$
(1)	(2)	deg	deg	km s^{-1}	Jy km s^{-1}	Jy km s^{-1}	$\log (M_{\odot})$	$\log (M_{\odot})$
(1)	(2)	(3)	(4)	(5)	(6)	(7)	(8)	(9)
J1603-53	J160305-531800	329.26	-0.52	5797	6.68 ± 1.15	3.93 ± 0.19	10.04	9.82
J1607-53	J160730-534932	329.40	-1.35	5497	7.75 ± 1.21	7.86 ± 0.57	10.07	10.07
J1605-51	J160544-511338	330.94	0.76	5723	10.63 ± 2.85	4.51 ± 0.28	10.24	9.86
J1612-52	J161245-524536	330.70	-1.10	5684	2.45 ± 0.90	2.97 ± 0.16	9.59	9.68
J1607-51	J160749-510452	331.28	0.65	6041	8.65 ± 1.51	8.77 ± 0.23	10.19	10.20
J1609-50	J161007-501128	332.15	1.06	6251	5.18 ± 2.01	5.33 ± 0.34	10.0	10.01
J1617-49	J161743-493216	333.49	0.69	2409	10.59 ± 1.76	11.35 ± 0.22	9.48	9.51
J1627-47	J162704-473758	335.93	0.94	7056	9.26 ± 1.28	7.53 ± 0.48	10.36	10.27
J1626-47	J162702-471646	336.18	1.19	7016	6.60 ± 1.17	4.35 ± 0.37	10.20	10.03
J1640-45	J164039-445933	339.46	1.01	4625	5.72 ± 1.55	3.69 ± 0.24	9.78	9.59
J1656-44	J165639-440511	341.99	-0.59	4903	10.04 ± 2.45	11.95 ± 0.46	10.07	10.15
J1657-45	J165744-451328	341.22	-1.45	6088	4.01 ± 1.22	2.87 ± 0.38	9.87	9.72
J1704-41	J170448-414022	344.81	-0.28	5525	5.44 ± 1.40	6.63 ± 0.33	9.91	10.00
J1705-40	J170527-405659	345.46	0.06	3920	4.61 ± 1.58	5.98 ± 0.36	9.54	9.65
J1713-40	J171314-405045	346.42	-1.06	6046	4.07 ± 1.19	3.99 ± 0.23	9.87	9.86
J1719-37	J171906-373147	349.78	-0.06	3411	3.05 ± 0.90	6.48 ± 0.46	9.24	9.57
J1758-21	J175830-215009	7.59	1.12	6909	5.87 ± 1.35	5.29 ± 0.40	10.14	10.10
J1808-21	J180808-213547	8.90	-0.71	1466	3.25 ± 1.00	2.22 ± 0.28	8.53	8.37
J1904+03A	J190412+030211	37.09	-1.45	3308	5.60 ± 0.84	3.93 ± 0.32	9.47	9.33
J1901+06	J190135+065133	40.19	0.88	2940	17.20 ± 2.58	14.55 ± 0.22	9.86	9.79
J1908+05	J190824+055946	40.20	-1.02	4565	5.97 ± 0.89	5.24 ± 0.13	9.79	9.74
J1906+07	J190640+073452	41.41	0.09	3097	5.16 ± 0.77	3.42 ± 0.41	9.38	9.21
J1914+10	J191500+101718	44.76	-0.48	637	20.60 ± 3.09	20.67 ± 0.55	8.63	8.60
J1912+13	J191236+132340	47.24	1.48	2764	7.09 ± 1.06	9.15 ± 1.07	9.43	9.54
J1919+14	J191957+140453	48.68	0.22	2797	13.70 ± 2.05	12.97 ± 1.27	9.72	9.69
J1921+14	J192135+145324	49.58	0.25	4075	6.56 ± 0.98	8.28 ± 0.40	9.73	9.83
J1918+16	J191846+161005	50.39	1.45	6630	7.08 ± 1.06	4.71 ± 0.30	10.19	10.01

conformed of 4 galaxies (see ‘Group B3’ in Fig. 12), while HIZOA J1811-21, HIZOA J1653-44, HIZOA J1721-37, and HIZOA J1716-35 are resolved into pairs of galaxies.

Table 2 lists the parameters of galaxies from both the HIZOA survey and the LV-SMGPS survey. For the flux verification, we only use HIZOA galaxies that have one counterpart in LV-SMGPS survey. This is illustrated in Fig. 3. The left panel of Fig. 3 displays the HIZOA flux versus LV-SMGPS flux. The red solid line indicates the $x=y$ line while the black dotted line indicates the linear regression. The slope for the linear regression is 1.18 ± 0.13 , which is consistent with slope 1 within $\sim 1.4 \sigma$ indicating that there is no systematic deviation between HIZOA and LV-SMGPS fluxes. The right panel in Fig. 3 shows the HI mass derived from the HIZOA flux versus the HI mass derived from the LV-SMGPS flux. We estimate the HI mass of HIZOA galaxies based on the luminosity distances that were calculated based on their heliocentric velocities to make it consistent with LV-SMGPS HI mass estimates. The black dotted line shows the linear regression with a slope of 0.989 ± 0.07 , which indicates that the HI masses measured from the HIZOA survey match well to those from the LV-SMGPS survey.

3 RESULTS

3.1 Large-scale structure

In this section, we investigate the large scale structures in and around the Local Void as uncovered by the LV-SMGPS

survey. Figure 4 (upper panel) displays the spatial distribution of HI detections in Galactic coordinates for $V_{\text{hel}} < 7500 \text{ km s}^{-1}$. The region explored with LV-SMGPS survey ($|b| < 1.5^\circ$) is marked by the black dotted rectangle and the circles inside this region represent SMGPS detections. The galaxies are colour coded by V_{hel} range, with blue, green, and red for $300 - 2500 \text{ km s}^{-1}$, $2500 - 5000 \text{ km s}^{-1}$, and $5000 - 7500 \text{ km s}^{-1}$ respectively. The lower panel of Fig. 4 shows the number of galaxies as a function of Galactic longitude, each bin consisting of $\Delta\ell = 8^\circ$. It is quite obvious that the galaxy density is considerably lower in the longitude range, $345^\circ < \ell < 35^\circ$ compared to other regions, especially for galaxies with V_{hel} below 5000 km s^{-1} – the region corresponding to the Local Void. These findings are consistent with Kraan-Korteweg et al. (2008), where they use HIZOA survey and find that LV consists of a huge under-dense region out to $V_{\text{hel}} \sim 6000 \text{ km s}^{-1}$ from about 345° to 45° in longitude and -30° to about $+45^\circ$ in latitude. Despite the significantly enhanced sensitivity and resolution of the LV-SMGPS survey in comparison to HIZOA, which enables the detection of low mass dwarfs (up to $10^8 M_{\odot}$ at 7500 km s^{-1}), we still find the LV to be under-dense. Nevertheless, the Void is not completely devoid of galaxies.

The number of galaxies in the region $329^\circ < \ell < 345^\circ$ is significantly higher compared to the other edge of the Void ($\ell > 35^\circ$). In particular, there is a high density of galaxies with V_{hel} ranging from 5000 km s^{-1} to 7500 km s^{-1} , possibly connecting with a part of the GA wall, also known as the Norma Wall or the Norma supercluster (Woudt & Kraan-

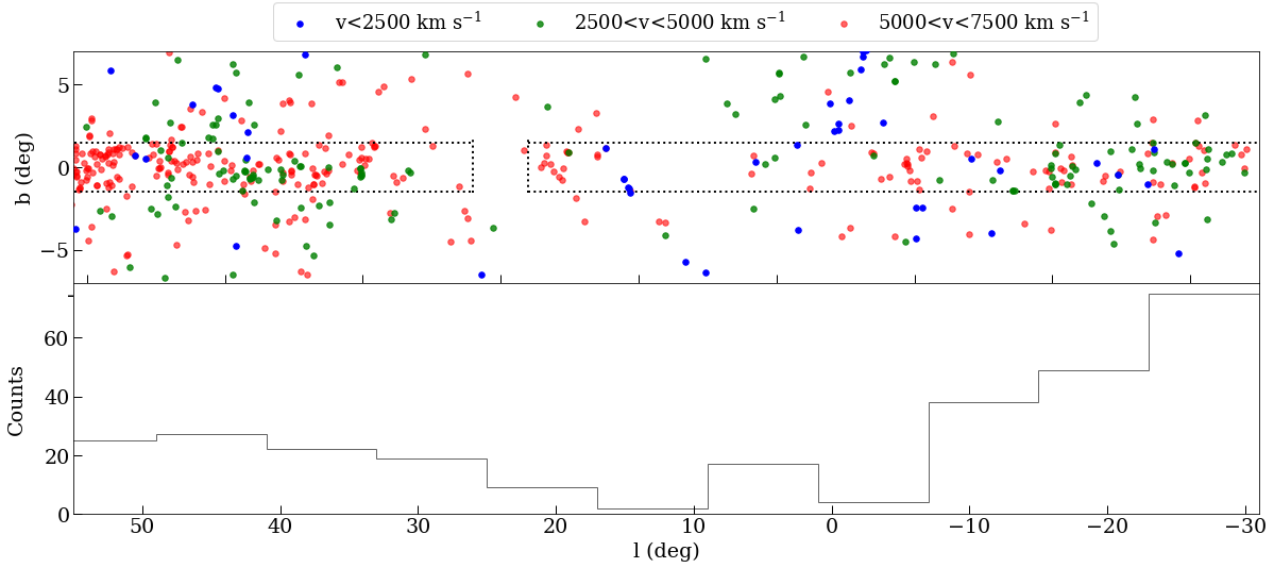


Figure 4. The distribution of galaxies in the Galactic coordinates. The region explored with LV-SMGPS survey is marked by the black dotted rectangles. The circles inside the rectangles ($-1.5 < b < 1.5$) represent the detections from the LV-SMGPS survey while the circles outside the rectangle ($b < -1.5; b > 1.5$) represent HIZOA only detections. The Galaxies are colour coded by velocity range, as follows: the $300 - 2500 \text{ km s}^{-1}$ velocity range is shown in blue, $2500 - 5000 \text{ km s}^{-1}$ in green, and $5000 - 7500 \text{ km s}^{-1}$ in red.

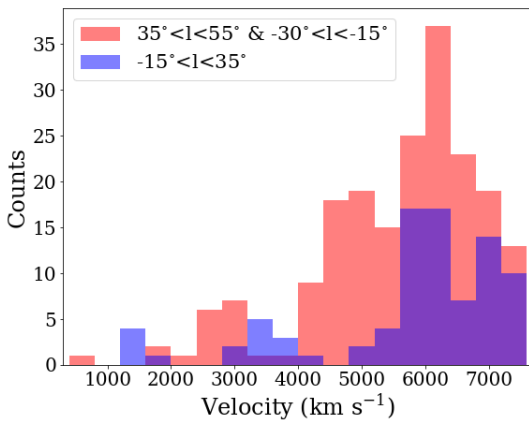


Figure 5. Histogram of velocities. The blue histograms represent the galaxies in the longitude range, $345^\circ < l < 35^\circ$ (LV) and the red histograms represent the longitude range, $329^\circ < l < 345^\circ$ and $35^\circ < l < 55^\circ$

Korteweg 2001; Woudt et al. 2004; Radburn-Smith et al. 2006; Staveley-Smith et al. 2016, Steyn et al. 2023).

In Fig. 5, we display the velocity histogram of the detections. The longitude range $345^\circ < l < 35^\circ$ dominated by void galaxies is shown by blue histograms since we find a lower galaxy density (a factor of 3.5 for galaxies with $V_{\text{hel}} < 6000 \text{ km s}^{-1}$) in this longitude range and the redshift distribution of galaxies from other regions ($329^\circ < l < 345^\circ$ and $35^\circ < l < 55^\circ$) is shown by red histograms. The velocity histograms (blue) of the LV show that the border of the Void is approximately around 6000 km s^{-1} .

Further, there seem to be peaks around $\sim 1500 \text{ km s}^{-1}$ and $\sim 3500 \text{ km s}^{-1}$ suggesting possible substructures in the Void. The velocity histograms of other regions (red) do not

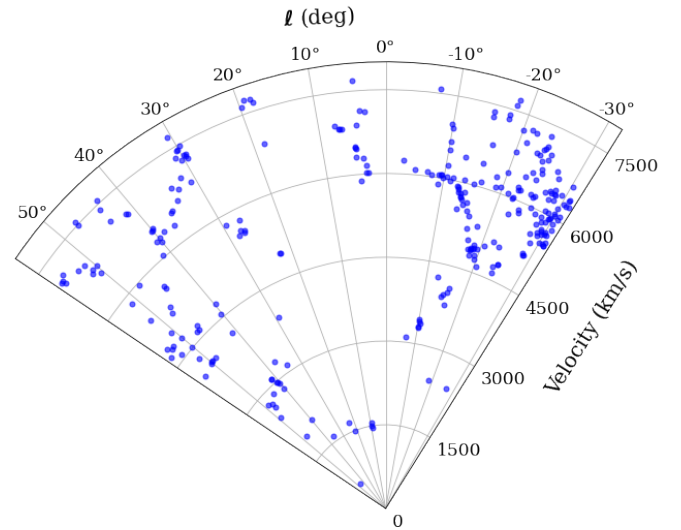


Figure 6. Redshift wedge of $\Delta b = 3^\circ$ along the Galactic longitude for the LV-SMGPS detections out to $V_{\text{hel}} < 7500 \text{ km s}^{-1}$.

have structure, except for a peak at $5500 - 6500 \text{ km s}^{-1}$ which is related to the GA overdensities.

3.2 The Local Void and its borders

Figure 6 displays the distribution of the detected galaxies in a redshift slice along Galactic longitudes for the width of the SMGPS, $|b| < 1.5^\circ$, out to the investigated volume of $V_{\text{hel}} < 7500 \text{ km s}^{-1}$. The distribution of HI detections is far from uniform, revealing various distinct features. The most

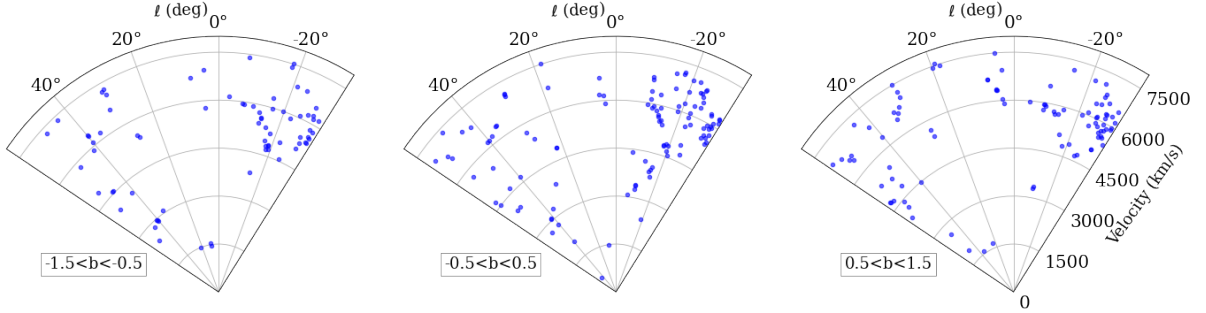


Figure 7. Redshift wedge plots for the HI detected galaxies in the LV-SMGPS survey in the latitude ranges $-1.5^\circ < b < -0.5^\circ$, $-0.5^\circ < b < 0.5^\circ$, and $0.5^\circ < b < 1.5^\circ$ respectively.

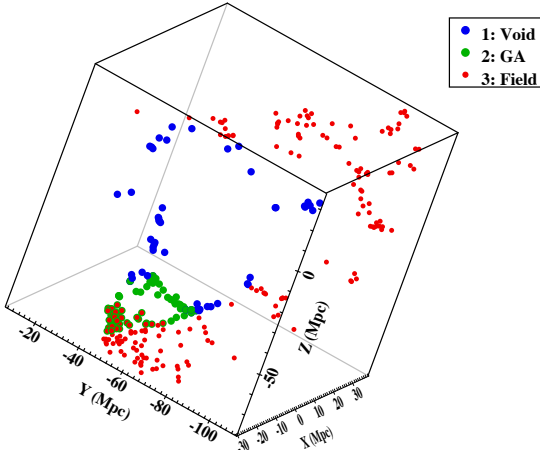


Figure 8. 3D distribution of galaxies in Cartesian coordinates. The blue circles represent the galaxies presumably residing in the LV (and its border), the red circles are galaxies beyond the Void, and the green circles are the galaxies that lie at the edge of Great Attractor wall.

prominent clearly is the LV, which at these low latitudes shows severe deficiency of galaxies in the region $-15^\circ < \ell < 35^\circ$ with $V_{\text{hel}} < 6000 \text{ km s}^{-1}$. In Fig. 7, the left, centre, and right panels show the distribution of the detected galaxies in a redshift slice in the latitude ranges, $0.5^\circ < b < 1.5^\circ$, $-0.5^\circ < b < 0.5^\circ$, and $-1.5^\circ < b < 1.5^\circ$ respectively. This demonstrates that the large scale structure is similar across the full width of the LV-SMGPS survey.

We now focus on the study the properties of galaxies as a function of local density, specifically categorizing galaxies based on their position i.e. whether they reside inside the Void, its border, or beyond the Void (hereafter referred to as the ‘field’). Hence, to classify LV-SMGPS detections into these three categories, we assess the boundary of LV. We consider all galaxies with velocities higher than 6000 km s^{-1} to be in average density environment since the Local Void border is approximately at around 6000 km s^{-1} (from Fig. 5). In addition, we consider all the galaxies in the longitude range, $40^\circ < \ell < 55^\circ$ to be of average density with the regular distribution of galaxies from $300 - 7500 \text{ km s}^{-1}$ as seen in Fig. 6. We convert the Galactic coordinates and the recession velocities into 3-D Cartesian coordinates to measure

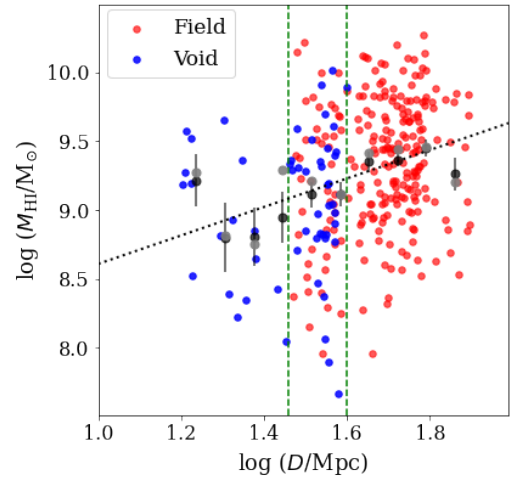


Figure 9. Log-log plot of HI mass versus the LV-centric distance. The Void and field galaxies are shown by blue and red circles. The green dashed lines represent the inner and outer border of Local Void. The black dotted line shows the linear regression over all galaxies. It has a slope of $\sim 1.03 \pm 0.21$. The black and grey circles represent the mean and median HI mass values per $\log D$ bin.

the actual distance between galaxies and allows us to classify Void galaxies, border galaxies, and field galaxies more quantitatively. Fig. 8 shows the 3D distribution of detected galaxies in Cartesian coordinates. The galaxy density in the central regions of the cube is very low, confirming the Local Void to be underdense. The blue circles represent the galaxies presumably within the Void, the red circles represent the galaxies residing in average density regions, and the galaxies that are at the edge of the GA wall are shown by green circles.

3.2.1 Extent of the LV at lowest latitudes

To determine the extent of the Void at the lowest Galactic latitudes, we estimate the centre of the Void as outlined by LV-SMGPS detections by assuming that it can be approximated reasonably well by the shape of a sphere. We calculate the centre of sphere by taking the centroid of centres of the opposite points of sphere lying on great circles within Fig.

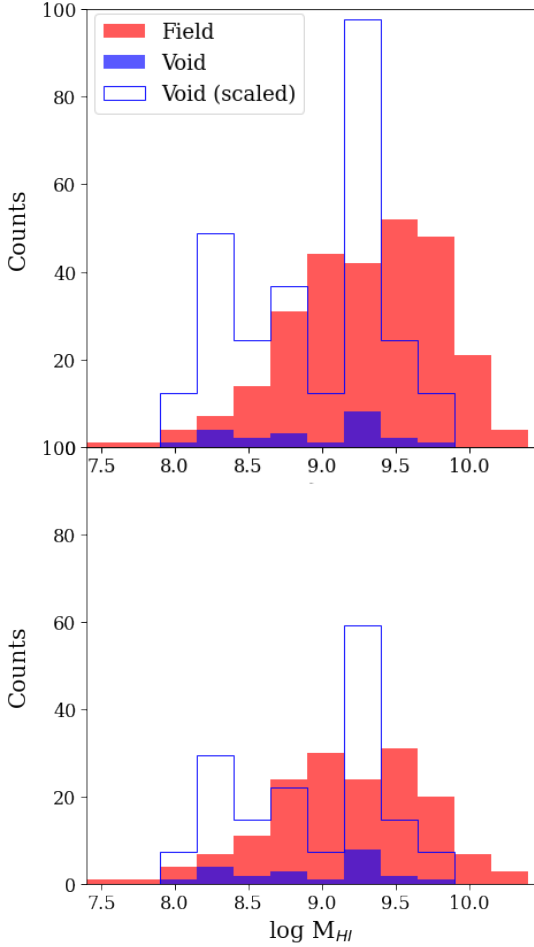


Figure 10. HI mass histograms for LV-SMGPS detections. The blue histograms represent the Void galaxies, red histograms the galaxies beyond the Void. Top panel: $V_{\text{hel}} < 7600 \text{ km s}^{-1}$. Bottom panel: $V_{\text{hel}} < 6000 \text{ km s}^{-1}$.

8. We compute the distance of each galaxy from the fiducial Void centre and check whether a sudden increase in galaxy count occurs beyond a specific radius. Additionally, we examine whether there is a trend between HI mass and the LV-centric radius.

In Fig. 9, we display the resulting log-log plot of HI mass ($\log M_{\text{HI}}$) versus the distance to the Void centre ($\log D$). The blue and red circles represent the galaxies presumably lying in Void and field respectively. The green dashed lines represent the inner (at $\log D = 1.46 \text{ Mpc}$) and outer ($\log D = 1.60 \text{ Mpc}$) boundaries of the LV. The density of galaxies inside the inner boundary is significantly lower compared to the density of galaxies outside this radius. This implies that the Void has a diameter of $\sim 58 \text{ Mpc}$. This is consistent with the estimated dimensions of the LV previously derived from cosmicflows-3, measuring roughly 69, 51, and 60 Mpc (Tully et al. 2019). The cosmicflows-3 study uses distances and inferred peculiar velocities of nearby galaxies to reconstruct the distribution of overdensities and underdensities in the nearby universe. We note that the LV doesn't have a simple shape (Rizzi et al. 2017; Tully et al. 2019)

We categorize galaxies according to their location with respect to the LV to study properties of galaxies as function

of environment. There are 17 galaxies deep in the Void, i.e. inside the inner boundary ($\log D < 1.46 \text{ Mpc}$), 96 galaxies are at the border of the Void, i.e. between inner and outer boundary of the Void ($1.46 \text{ Mpc} < \log D < 1.60 \text{ Mpc}$), and the remaining 178 galaxies are in field, i.e. beyond the Void ($\log D > 1.60 \text{ Mpc}$).

3.3 HI mass variation with environment

In this section, we investigate the HI mass as a function of LV-centric radius. In Fig. 9, we display $\log M_{\text{HI}}$ versus the $\log D$. The black dotted line shows the linear regression of all galaxies with a slope of $\sim 1.03 \pm 0.21$. The linear regression has a large scatter ~ 0.4 . The black and grey circles represent the mean and median HI mass values. The distribution of the points in Fig. 9 reveals tendency of the HI mass with LV-centric radius. The trend is also clear in the points of the outer envelopes of the distribution along $\log D$. To assess the validity of this trend, we use the Spearman rank correlation coefficient and Pearson correlation coefficient to analyze the relation between the HI mass and the LV-centric radius. The Pearson correlation coefficient measures the strength of the linear monotonic correlation between two sets of data while the Spearman's correlation estimates the strength of monotonic relationships, regardless of whether they are linear or not. We calculated the Spearman's correlation coefficient and Pearson correlation coefficient and we find them to be very similar. We find that the Spearman correlation coefficient is 0.255 (p value $\sim 1.3 \text{ e}^{-5}$) and the Pearson correlation coefficient to be 0.251 (p value $\sim 1.4 \text{ e}^{-5}$), which means that the HI mass and LV-centric radius are weakly correlated, but with a high significance. We divided the data into several sections with bin size 0.08 and the average/median value of each bin is marked in grey/black circles in Fig. 9. The binned Spearman and Pearson correlation coefficients for the mean values are 0.90 (p value $\sim 9 \text{ e}^{-4}$) and 0.91 (p value $\sim 6 \text{ e}^{-4}$) and the binned Spearman and Pearson correlation coefficients for the median values are 0.63 (p value ~ 0.06) and 0.73 (p value ~ 0.026). The correlation appears to be much stronger in the binned data sets.

As a further assessment of the HI mass dependency of local density, i.e. environment, we consider the HI mass distribution of Void galaxies with $\log(D/\text{Mpc}) < 1.46$, and galaxies at the border of Void and beyond Void with $\log(D/\text{Mpc}) > 1.46$. We test whether there are differences in HI mass distributions within the Void compared to those beyond the Void. The top panel in Fig. 10 shows the HI mass histogram of all detected galaxies. Void galaxies are represented by blue and galaxies beyond the Void are represented by red histograms. The average HI mass of Void galaxies is $\sim 10^{8.93} M_{\odot}$ while the average HI mass of galaxies in average density regions is $\sim 10^{9.3} M_{\odot}$, corresponding to a difference of $\sim 0.4 \text{ dex}$. We perform a Kolmogorov-Smirnov (KS) test which gives a probability of 0.015 for the galaxies in this Void and beyond the Void being drawn from the same distribution. The test implies a difference at the 2.5σ level, which is not statistically significant. However, the samples probe different volumes: LV $< 6000 \text{ km s}^{-1}$, while the whole sample is delimited by 7500 km s^{-1} . We reinvestigate by adopting the same volume limit. Therefore, we remove all the galaxies with velocities higher than 6000 km s^{-1} from the sample

of field galaxies to keep same redshift range for Void galaxies and galaxies beyond the Void to compare their HI mass distributions. In the bottom panel of Fig. 10, we show the HI mass of detected galaxies with $V_{\text{hel}} < 6000 \text{ km s}^{-1}$. The average HI mass of galaxies beyond the Void is $\sim 10^{9.18} M_{\odot}$ corresponding to a difference of ~ 0.25 dex between Void galaxies and field. The KS test gives a p value of ~ 0.14 for both the galaxies in the Void and beyond Void to be drawn from the same distribution. This does not support the hypothesis that the two samples are being drawn from different populations.

However, it should be highlighted that the Void doesn't host any massive galaxies, i.e. galaxies with $M_{\text{HI}} > 10^{9.7} M_{\odot}$. Moreover, the number of galaxies drops significantly for galaxies with HI mass higher than $10^{9.4} M_{\odot}$. This is consistent with results from studies that reconstruct the cosmic web using spectroscopic or photometric redshifts, which show that galaxies with high stellar mass are more likely to be located closer to filaments and walls than their less massive counterparts in low-density regions (Chen et al. 2017; Kraljic et al. 2018; Laigle et al. 2018; Lubert et al. 2019). The observed correlation between HI mass and stellar mass (Parkash et al. 2018; Catinella et al. 2018) further points to an expectation of fewer galaxies with higher HI masses in voids, in agreement with our results. Furthermore, our results are also consistent with the numerical simulations that predict that the mass function in voids is steeper than in walls and filaments, i.e. the number of massive haloes is depressed compared to that of the low mass haloes (Gottlöber et al. 2003; Alfaro et al. 2020; Habouzit et al. 2020; Rosas-Guevara et al. 2022).

4 CLUSTERING OF HI SELECTED VOID GALAXIES

The galaxy clustering was found to be a strong function of environment (e.g. Abbas & Sheth 2007; Pujol et al. 2017; Paranjape et al. 2018). In the context of hierarchical cosmological structure formation scenario, voids are expected to have a substructure consisting of sub voids, tendrils, filaments, etc (van de Weygaert & van Kampen 1993; Sheth & van de Weygaert 2004; van de Weygaert & Platen 2011; Aragon-Calvo & Szalay 2013; Crone Odekon et al. 2018). Hence, void galaxies are not necessarily isolated at small scales ($\lesssim 1$ Mpc) but their density of galaxies is very low on the scale of voids. The small scale clustering of galaxies in voids was not found to differ from clustering of galaxies in average density environments. For example, Szomoru et al. (1996) found that the clustering of HI detected galaxies within 1 Mpc of galaxies in the void is similar to clustering in average density regions (within a factor of two). Abbas & Sheth (2007) study environmental dependence of clustering for galaxies in the Sloan Digital Sky Survey (SDSS) and they find that the relation between clustering strength and density is not monotonic. They find that galaxies in the void centers are more clustered than those in the void outskirts, but the latter are less clustered than those at moderate overdensities.

Pustilnik & Tepliakova (2011) and Pustilnik et al. (2019) studied clustering of optically selected void galaxies and they find that around 17.5 percent of the void galaxies form pairs, triplets, quadruplets or larger groups.

Kreckel et al. (2012) observed 55 galaxies ($-16^m.1 > M_r > -20^m.4$) in voids using the Westerbork Synthesis Radio Telescope (WSRT). They detect HI in 41 of the galaxies and they identify 18 HI rich companions in pairs/triplets, a total of 34 out of 59 $\sim 57\%$, and they suggest that the small-scale clustering of galaxies in voids is very similar to that in higher density regions. They have used sky separations of 600 kpc and velocity differences of 200 km s^{-1} due to their observational constraints. Kurapati (2020) obtained HI observations of 24 dwarf galaxies ($M_B > -16 \text{ mag}$) in the Lynx-Cancer void and they find that 13 galaxies of 31 (including previous detections) i.e. 42% were part of pairs or triplets.

4.1 Clustering in LV and its surroundings

We use the LV sample to study the clustering properties of HI selected galaxies. We compare the small-scale clustering for galaxies residing in different local densities: the least dense regions (deep in LV), moderately underdense regions (border of the LV), average density regions (field excluding GA wall), and moderately overdense regions (GA wall). Galaxies within the region of the GA wall (as seen in Fig. 8) are categorized as being in a moderately overdense region, as the density of galaxies is clearly higher compared to regions with average density (see Fig. 6). For the remaining galaxies, we have used the categorization approach described in section §3.2.1, based on the LV-centric distance, which divides galaxies into those deeply embedded within the Void ($\log D < 1.46$), those on the border of the Void ($1.46 < \log D < 1.60$), and galaxies in the field ($\log D > 1.60$).

We use sky separations of 600 kpc and velocity differences of 200 km s^{-1} to study the small scale clustering of HI selected void galaxies to enable a direct comparison with previous studies (Kreckel et al. 2012; Kurapati 2020). If we consider only the galaxies that are in deep in the LV ($\log D < 1.46$ in Fig. 9), there are a total of 17 galaxies and 8 galaxies ($\sim 47\%$) within 600 kpc and 200 km s^{-1} , with 6 of them having one neighbour, one with two neighbours, six with three neighbours, and two with four neighbours within 600 kpc and 200 km s^{-1} which is consistent with the previous studies (Kreckel et al. 2012; Kurapati 2020).

We find that 22 out of 60 galaxies ($\sim 36.6\%$) at the border of the Void and 26 out of 134 galaxies ($\sim 19.4\%$) in the field (excluding the GA wall) are found within 600 kpc and 200 km/s , both of which show lower clustering compared to the clustering in the Void center. On the other hand, for a total of 80 galaxies in the GA wall, 43 ($\sim 53.8\%$) were observed within 600 kpc and 200 km s^{-1} . This is higher than the small-scale clustering close to the Void center and its outskirts, as well as the field. This indicates that the small-scale clustering of the least dense regions (i.e center of LV) is higher than that of moderately underdense regions (LV border and field), but is lower than the small-scale clustering of the moderately overdense regions (GA wall). This is in agreement with Abbas & Sheth (2007), who found that the galaxies in the least dense regions are more clustered than galaxies in moderately underdensities, but galaxies in moderate underdensities are less clustered than those at moderate overdensities.

Table 3. HI parameters of galaxies in groups.

Group	Region	No	Name	ℓ	b	V_{hel}	w_{20}	w_{50}	$\log(M_{\text{HI}})$	$\log(M_{\text{dyn}})$	$\log(M_{\text{halo}})$	S	d_{proj}
(1)	(2)	(3)	SMGPS-HI-	deg	deg	km s^{-1}	km s^{-1}	km s^{-1}	$\log(M_{\odot})$	$\log(M_{\odot})$	$\log(M_{\odot})$	(13)	kpc
(1)	(2)	(3)	(4)	(5)	(6)	(7)	(8)	(9)	(10)	(11)	(12)	(13)	(14)
F1	Field	a	J160121-532553	328.98	-0.45	5477	245	194	9.44	10.49			
		b	J155952-530455	329.04	-0.04	5545	340	281	9.83	11.20	11.34	0.028	577
		c	J160114-531146	329.12	-0.26	5487	129	113	8.91	10.48			
F2	Field	a	J161709-521624	331.52	-1.21	5162	207	167	9.58	10.48			
		b	J161621-520100	331.61	-0.94	5160	87	72	8.76	9.75	10.70	0.037	371
		c	J161738-520111	331.75	-1.08	5189	127	95	9.15	10.17			
F3	Field	a	J160803-505214	331.45	0.78	6290	136	114	9.27	10.18			
		b	J160728-503434	331.58	1.06	6385	89	74	8.99	9.63			
		c	J160942-503349	331.85	0.83	6391	179	164	9.64	10.57			
		d	J160914-501912	331.96	1.06	6456	164	127	9.91	11.24	12.01	0.028	1399
		e	J161007-501128	332.15	1.06	6251	223	185	10.01	11.79			
		f	J161210-501742	332.32	0.76	6384	267	232	9.71	11.25			
B1	Border	a	J165630-445219	341.36	-1.06	4895	85	70	9.23	9.57			
		b	J165259-441844	341.40	-0.22	4929	138	138	8.99	10.12			
		c	J165323-441909	341.44	-0.28	4973	314	287	10.22	11.56			
		d	J165549-441534	341.76	-0.58	4896	134	71	8.82	9.58	11.86	0.036	1407
		e	J165633-442106	341.77	-0.74	4776	176	162	9.36	10.36			
		f	J165639-440511	341.99	-0.59	4903	356	324	10.15	11.47			
		g	J165608-440041	341.99	-0.47	4870	184	165	9.40	10.47			
		h	J165852-435329	342.39	-0.78	4868	46	46	8.37	9.41			
B2	Border	a	J171053-402428	346.51	-0.44	5730	65	45	8.66	9.22			
		b	J171120-402132	346.60	-0.48	5755	93	72	8.29	9.11	9.81	0.016	288
		c	J171150-401947	346.68	-0.54	5795	93	58	8.93	9.54			
V1	Void	a	J172253-383451	349.34	-1.27	3380	91	77	8.52	9.46			
		b	J171906-373147	349.78	-0.06	3411	126	82	9.57	10.11			
		c	J172058-374204	349.85	-0.46	3448	163	124	9.27	10.47	11.06	0.013	1100
		d	J172109-374256	349.86	-0.50	3319	219	191	9.52	10.63			
		e	J172031-373608	349.88	-0.33	3298	127	112	9.19	10.44			
B3	Border	a	J175258-242216	4.76	0.94	6459	266	224	10.21	11.61			
		b	J175320-241850	4.85	0.90	6477	186	163	9.68	10.66			
		c	J175330-241811	4.88	0.87	6325	186	139	9.46	10.41	11.71	0.54	225
		d	J175325-241645	4.89	0.90	6508	163	139	9.58	10.47			
V2	Void	a	J180808-213547	8.90	-0.71	1466	88	69	8.37	9.53			
		b	J181051-213408	9.23	-1.25	1564	337	288	8.80	11.12	11.17	0.02	320
		c	J181149-213318	9.35	-1.44	1511	183	142	8.83	10.07			
F4	Field	a	J192836+195742	54.84	1.18	7076	241	191	9.84	10.91			
		b	J192745+200537	54.86	1.42	7005	135	99	9.06	9.90	10.98	0.008	923
		c	J192956+200923	55.16	1.00	7079	93	83	8.89	9.68			

4.2 Potential galaxy groups

Voids are expected to exhibit intricate fine substructure consisting of sub-voids, tendrils, filaments. Numerical simulations predict that galaxies in voids preferentially lie within the filamentary void substructures. In fact, some earlier observational studies have found indications for such filamentary substructure in voids (e.g. [Zitrin & Brosch 2008](#); [Beygu et al. 2013](#)). For example, [Beygu et al. \(2013\)](#) reported three interacting galaxies embedded in a common HI envelope, which they hypothesized to be an assembly of a filament in a void. [Chengalur et al. \(2017\)](#) find an approximately linearly aligned triplet of gas-rich dwarfs with large-scale velocity continuity, which they argue is consistent with the galaxies lying along a filament. This can be interpreted as a consequence of the structure formation proceeding more slowly.

To explore if we find filamentary substructures in the LV, we search for galaxy group candidates in the LV–SMGPS data. We mainly use the projected separation be-

tween galaxies and the difference between recession velocities for the identification of groups. We find a total of nine possible groups, some of these are tight groups, while others may still be in the process of assembling. Figure 11 shows the position of the potential groups in a redshift wedge. The blue dots represent galaxies residing deep in the Void ($\log D < 1.46$), magenta the galaxies at the border of Void ($1.46 < \log D < 1.60$) while red indicates the galaxies in field ($\log D > 1.60$; see Fig. 9). Galaxies conforming potential groups are marked in green. Two of the groups (with 5 and 3 members) are located in the LV, three of them (with 8, 4, and 3 members respectively) lie at the border of the LV, and the other four (6 and 3 members) are found in the field. The velocities of the group members all lie within 200 km s^{-1} .

We estimate the dynamical mass of each group member following [de Blok & Walter \(2014\)](#) using

$$M_{\text{dyn}} = \frac{R}{G} \left(\frac{w_{50}}{2 \sin i} \right)^2, \quad (1)$$

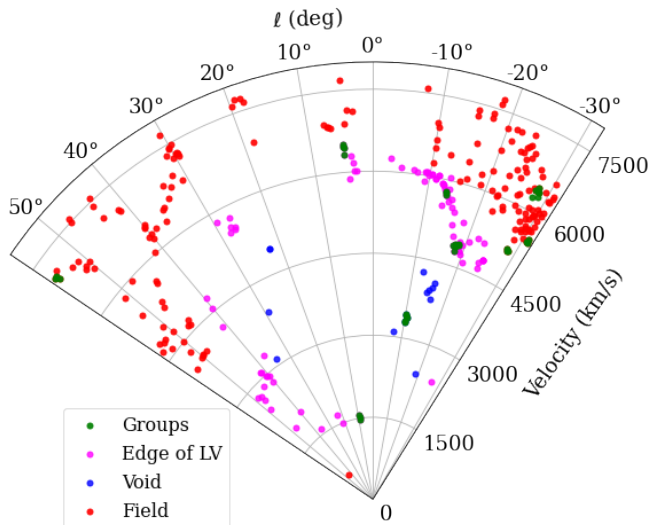


Figure 11. Redshift wedge for the LV-SMGPS detections. The blue circles represent the galaxies residing deep within the LV ($\log D < 1.46$), magenta galaxies at the border of LV ($1.46 < \log D < 1.60$), and red field galaxies. The galaxies residing in groups of galaxies are marked in green.

where R and i are radius of the HI disc and inclination angle of galaxy. The inclination angle is determined by using $\cos^2(i) = (b^2 - \theta_b^2)/(a^2 - \theta_a^2)$, where a and b are the major and minor axis of the galaxy, θ_a and θ_b are the sizes of the synthesis beam.

To quantify the compactness of groups, we define the compactness parameter, S , following Duplancic et al. (2017),

$$S = \sum_{i=1}^N \frac{R^2}{(d_{\text{proj}}/2)^2}, \quad (2)$$

where N is the number of galaxies in the group and d_{proj} is the maximum distance between group members. Duplancic et al. (2013, 2017) have adopted a threshold $S > 0.03$ which corresponds to compactness of compact groups of galaxies. But, we note that they used optical diameters and here we are using HI diameter.

Table 3 lists the HI parameters of galaxies residing in groups. The columns are as follows:

- Column 1 - Name of group
- Column 2 - Environment in which group was found
- Column 3 - Group member identifier
- Column 4 - Name of galaxy, LV-SMGPS identifier giving RA and Dec
- Column 5 and 6 - Galactic longitude (deg) and latitude (deg)
- Column 7 - Optical heliocentric velocity, V_{hel} in km s^{-1}
- Column 8 and 9 - Line widths w_{50} and w_{20} in km s^{-1}
- Column 10 - HI mass in $\log M_{\odot}$
- Column 11 - Dynamical mass in $\log M_{\odot}$
- Column 12 - Total dynamical mass of the group in $\log M_{\odot}$
- Column 13 - Compactness parameter, S .
- Column 14 - Maximum projected distance between the

members of group, d_{proj} .

4.2.1 Groups in the Void (V1–V2)

Figure 12 displays all the galaxy group candidates in the Void and at the border of Void. The top row (12a) shows the HI intensity map of the group V1 which contains 5 galaxies. The left panel shows all 5 galaxies within one panel. The maximum projected distance (d_{proj}) between the group members is ~ 1.1 Mpc. It has a fairly compact core (see box) with $d_{\text{proj}} \sim 142.5$ kpc. The next two panels show the HI morphologies and the velocity fields of the group galaxies. The galaxies are at their actual position but are magnified by a factor of five to visualize the details of their HI distribution. The left panel of second row (12b) shows the HI intensity map and velocity field of a group of 3 galaxies in the Void. The HI morphology of the galaxy J181051-213408 is peculiar, it is in the form of a HI ring with a tail like feature in the north. The maximum projected distance between the galaxies is 320 kpc. The approximately linear alignment of the galaxies in these groups (the compact core of V1 and the 3 galaxies of group V2) resembles galaxies arranged along intra-void filaments, which could signify the ongoing growth of these galaxies along a filament inside the LV.

4.2.2 Groups at the edge of the Void (B1–B3)

We identified three possible groups at the borders surrounding the Void. The group with the highest number of members, B1 with 8 galaxies is displayed in the third row (12d) of Fig. 12. The first panel is at fixed original scale. A zoom-in of the region outlined by a box is shown in the next panel. It is a very extended galaxy (J165323-441909) of diameter ~ 80 kpc and has a close companion (J165259-441844) at a projected distance of ~ 35 kpc. The galaxy, J165323-441909 has a tail extending in the south direction, possibly due to gas accretion from an intra-void filament or due to a gas-rich minor merger. The third and fourth panel show the full group with magnified HI maps. The close companion galaxy, J165259-441844 is shown by ‘X’ as it is not visible in the magnified HI map. The maximum projected distance between these galaxies is ~ 1.4 Mpc within 200 km s^{-1} . However, the group of four galaxies (J165608-440041, J165639-440511, J165549-441534, and J165633-442106) within B1 is within ~ 424 kpc. The close proximity in space and redshift may suggest that majority of these are group members, however, a few galaxies could be in the process of joining the system.

The right panel of second row (Fig. 12c) shows group B2 of three galaxies at the edge of the Void, with $d_{\text{proj}} \sim 287$ kpc. Although not located within the Void but at its borders, the image also reveals a linear alignment of galaxies with large scale velocity continuity, consistent with galaxies lying along a filament.

The bottom row (12e) shows their HI distribution (morphology and velocity field) of a compact group B3, which consists of four galaxies at the original scale. It was originally detected as a single massive galaxy in the HIZOA survey (HIZOA J1753-24A). The maximum projected distance between the members of this group is around ~ 225

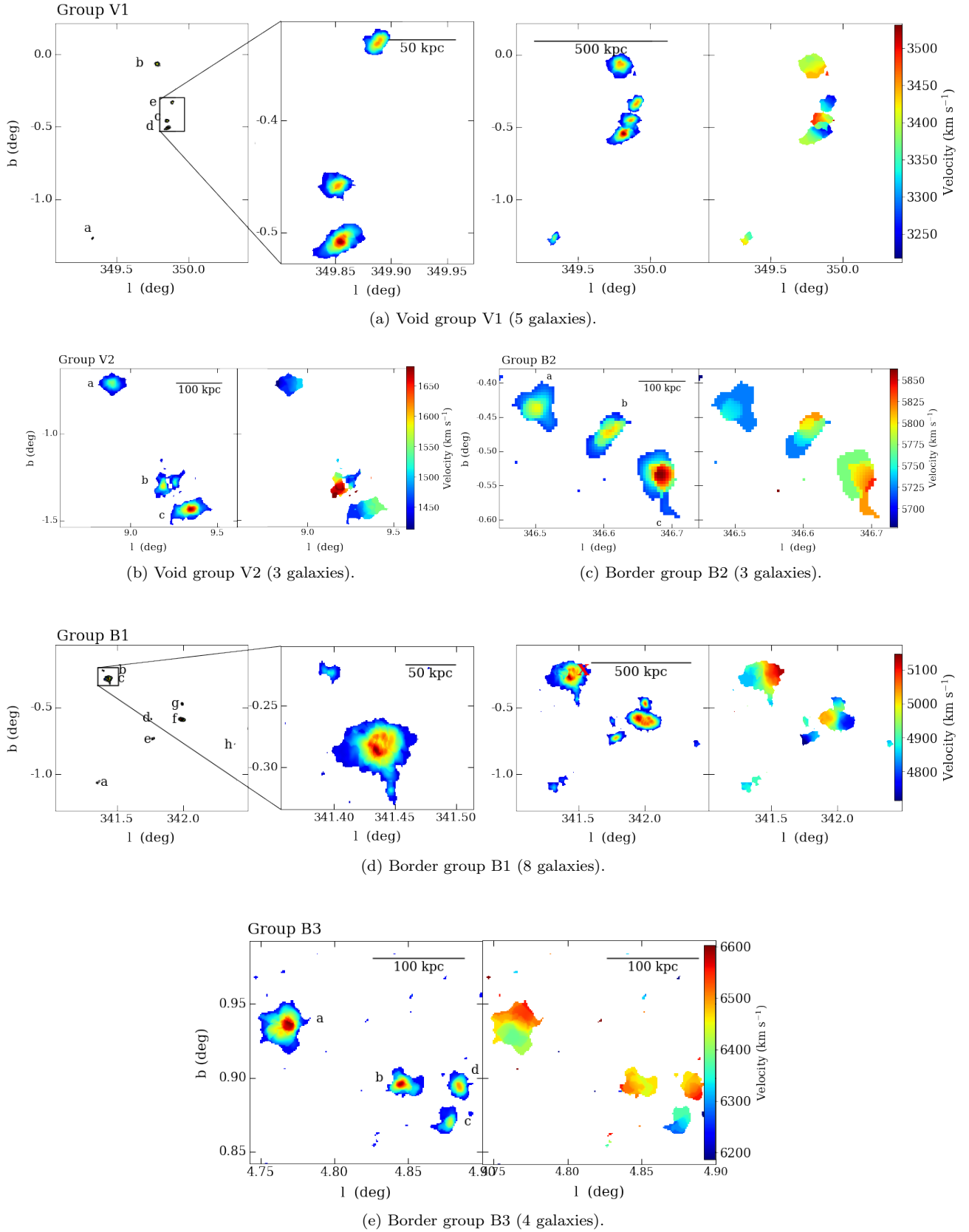


Figure 12. Galaxy groups in Void and border of Void.

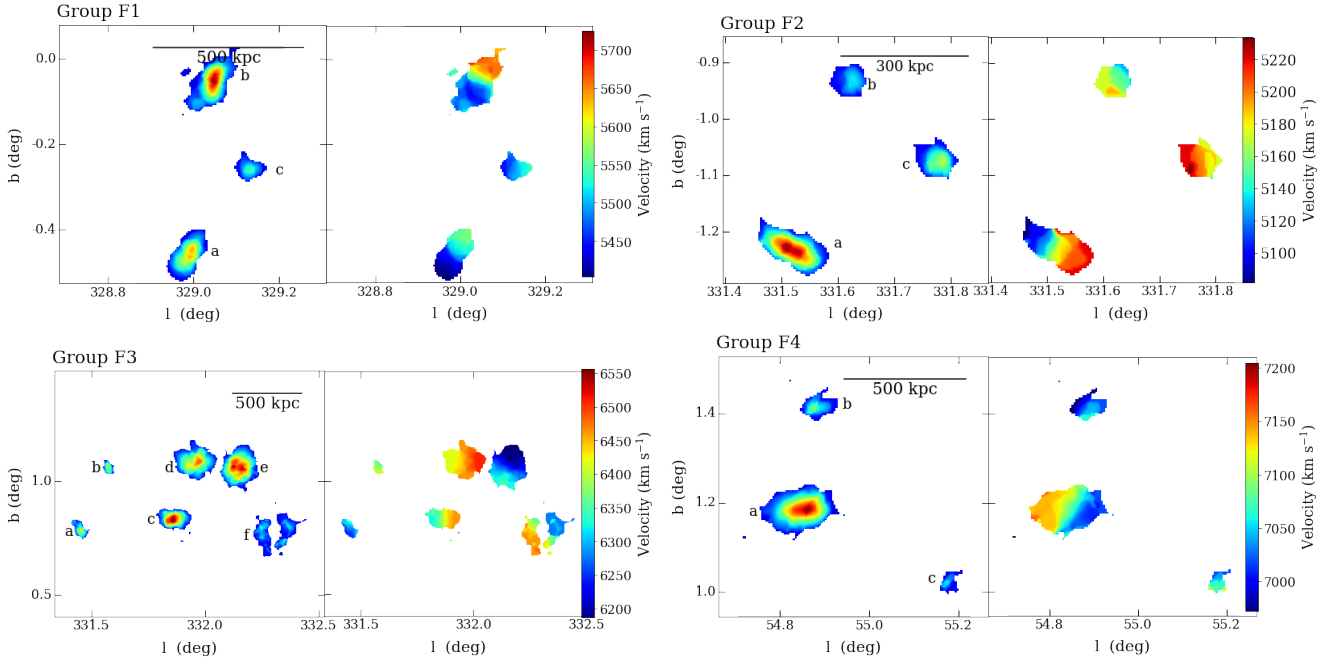


Figure 13. Upper panel: Loose group of 3 galaxies in average density environment (towards the edge of Great Attractor). Lower panel: Loose group of 3 galaxies in average density environment. The galaxies are located at the proper position, but are magnified by a factor of five to reveal the details of HI distribution.

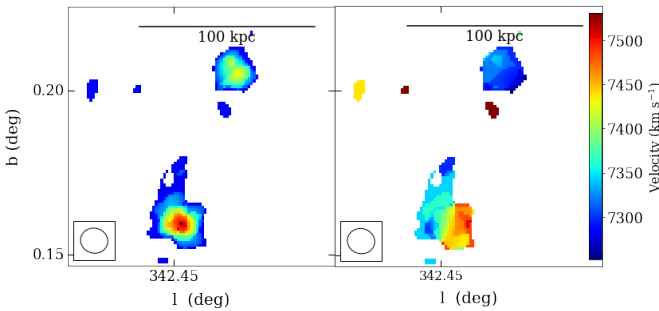


Figure 14. Pair of galaxies in average density environment.

kpc. The group of three galaxies (J175320-241850, J175325-241645, and J175330-241811) in the lower right is much more compact with the maximum projected distance of just ~ 68 kpc.

4.2.3 Groups in field (F1–F4)

The four candidates for groups of galaxies in average density regions are given in Fig. 13. In all the panels, the galaxies are at their actual position but are magnified by a factor of five to visualize the details of their HI distribution. Groups F1 (top left), F2 (top right), and F4 (bottom right) have 3 members each. Group F3 (bottom left) contains 6 galaxies, with $d_{proj} \sim 1.4$ Mpc. However, no further substructure was notable ($d_{proj} < 500$ kpc). The HI morphology of galaxy, J161210-501742 in this group is very interesting. It shows a HI ring with ~ 65 kpc diameter. The ring galaxies could have various origins such as collisional origin with an intruder galaxy (e.g. Bait et al. 2020). However, it is difficult to comment on the formation scenario of this ring galaxy as

we do not have observations in optical/infrared wavelengths given its location in the ZoA and we did not find any nearby companions for this ring galaxy.

Group F1 (top left) and Group F2 (top right) have three members and lie in the vicinity of the Great Attractor wall, with $d_{proj} \sim 578$ and 371 kpc respectively. Group F4 also has three members with $d_{proj} \sim 923$ kpc. These could be loose group of galaxies that may still be in the process of forming themselves.

We also found a close pair of galaxies (Fig. 14) in the field with offsets of only 100 kpc and 100 km s $^{-1}$. We haven't found any compact groups (with $d_{proj} < 350$ kpc) in average density environments in contrast to Void and the border of Void.

5 SUMMARY AND CONCLUSIONS

We used the HI 21 cm emission observations from the LV-SMGPS to study the HI galaxy population in and around the LV along the inner Zone of Avoidance ($|b| < \pm 1.5^\circ$), including their HI properties as a function of local environment. We detected and parameterised 291 galaxies and categorized the galaxies based on their environment. We find that 17 of the detected galaxies lie deep inside the LV, 96 galaxies are at the border of the LV, while the remaining 178 galaxies are in average density environments. The extent of the Void as traced by LV-SMGPS is ~ 58 Mpc. It is severely under-dense over the longitude range $35^\circ < \ell < 35^\circ$, $-1.5^\circ < b < 1.5^\circ$, up to redshift $z < 4500$ km s $^{-1}$. We found that the HI mass and LV-centric radius are weakly correlated, but with a high significance. However, number statistics in voids are of course very low.

We find a total of 9 group candidates two of which (one

with 5 members and one with 3 members) are inside the Void. Three groups (with 8, 4, and 3 members respectively) form part of the border of Void and four of them (one with 6, three with 3 members) are in average density regions. Some groups in and at the edge of the Void are consistent with galaxies lying along intra-void filaments, which may suggest the ongoing growth of these galaxies along a filament inside the Void.

These results are consistent with other studies that observe voids containing a population of galaxies some of which present evidence for ongoing gas accretion, interactions with small companions and filamentary alignments (e.g. Kreckel et al. 2011, 2012; Beygu et al. 2013; Chengalur & Pustilnik 2013; Chengalur et al. 2015, 2017; Kurapati 2020). The small-scale clustering of the HI selected galaxies at the centre of the Void is higher than that of clustering in outskirts of the Void and the field excluding the GA wall, but is lower than clustering in relatively overdense GA wall. This is in agreement with Abbas & Sheth (2007), who found that the galaxies in least dense regions are more clustered than galaxies in moderately underdensities, but galaxies in moderate underdensities are less clustered than those at moderate overdensities.

ACKNOWLEDGEMENTS

We thank the anonymous referee for insightful comments that improved this paper. SK, RKK, and DJP greatly acknowledge support from the South African Research Chairs Initiative of the Department of Science and Technology and National Research Foundation.

The MeerKAT telescope is operated by the South African Radio Astronomy Observatory, which is a facility of the National Research Foundation, an agency of the Department of Science and Innovation. We acknowledge the use of the ilifu cloud computing facility—www.ilifu.ac.za, a partnership between the University of Cape Town, the University of the Western Cape, the University of Stellenbosch, Sol Plaatje University, the Cape Peninsula University of Technology, and the South African Radio Astronomy Observatory. The Ilifu facility is supported by contributions from the Inter-University Institute for Data Intensive Astronomy (IDIA a partnership between the University of Cape Town, the University of Pretoria, the University of the Western Cape and the South African Radio Astronomy Observatory), the Computational Biology division at UCT and the Data Intensive Research Initiative of South Africa (DIRISA).

DATA AVAILABILITY

The full galaxy catalogue and the atlas are available online. The ASCII file of the GPS catalogue will be submitted to SIMBAD. The raw MeerKAT data are archived and are available at <https://archive.sarao.ac.za>. Reduced data cubes will be available on request.

SUPPORTING INFORMATION

Supplementary data are available online at MNRAS. The full LV-SMGPS catalogue is provided in machine-readable

format as Catalogue.txt, and the complete LV-SMGPS atlas is accessible as atlas.pdf.

REFERENCES

- Abbas U., Sheth R. K., 2007, *MNRAS*, **378**, 641
- Alfaro I. G., Rodriguez F., Ruiz A. N., Lambas D. G., 2020, *A&A*, **638**, A60
- Alpaslan M., et al., 2014, *MNRAS*, **440**, L106
- Anand G. S., Rizzi L., Tully R. B., 2018, *AJ*, **156**, 105
- Aragon-Calvo M. A., Szalay A. S., 2013, *MNRAS*, **428**, 3409
- Bait O., Kurapati S., Duc P.-A., Cuillandre J.-C., Wadadekar Y., Kamphuis P., Barway S., 2020, *MNRAS*, **492**, 1
- Beygu B., Kreckel K., van de Weygaert R., van der Hulst J. M., van Gorkom J. H., 2013, *AJ*, **145**, 120
- Blanton M. R., Eisenstein D., Hogg D. W., Schlegel D. J., Brinkmann J., 2005, *ApJ*, **629**, 143
- Catinella B., et al., 2018, *MNRAS*, **476**, 875
- Chen Y.-C., et al., 2017, *MNRAS*, **466**, 1880
- Chengalur J. N., Pustilnik S. A., 2013, *MNRAS*, **428**, 1579
- Chengalur J. N., Pustilnik S. A., Makarov D. I., Perepelitsyna Y. A., Safonova E. S., Karachentsev I. D., 2015, *MNRAS*, **448**, 1634
- Chengalur J. N., Pustilnik S. A., Egorova E. S., 2017, *MNRAS*, **465**, 2342
- Crone Odekon M., Hallenbeck G., Haynes M. P., Koopmann R. A., Phi A., Wolfe P.-F., 2018, *ApJ*, **852**, 142
- Croton D. J., Farrar G. R., 2008, *MNRAS*, **386**, 2285
- Croton D. J., et al., 2005, *MNRAS*, **356**, 1155
- Dekel A., Zolotov A., Tweed D., Cacciato M., Ceverino D., Primack J. R., 2013, *MNRAS*, **435**, 999
- Donley J. L., et al., 2005, *AJ*, **129**, 220
- Duplancic F., O’Mill A. L., Lambas D. G., Sodr e L., Alonso S., 2013, *MNRAS*, **433**, 3547
- Duplancic F., Alonso S., Coldwell G., Garcia Lambas D., 2017, *Boletín de la Asociacion Argentina de Astronomia La Plata Argentina*, **59**, 121
- Ekta Chengalur J. N., Pustilnik S. A., 2008, *MNRAS*, **391**, 881
- Goldberg D. M., Vogeley M. S., 2004, *ApJ*, **605**, 1
- Gottl ber S., Lokas E. L., Klypin A., Hoffman Y., 2003, *MNRAS*, **344**, 715
- Habouzit M., Pisani A., Goulding A., Dubois Y., Somerville R. S., Greene J. E., 2020, *MNRAS*, **493**, 899
- Heywood I., et al., 2022, *ApJ*, **925**, 165
- Hoyle F., Rojas R. R., Vogeley M. S., Brinkmann J., 2005, *ApJ*, **620**, 618
- Hoyle F., Vogeley M. S., Pan D., 2012, *MNRAS*, **426**, 3041
- Jian H.-Y., et al., 2022, *ApJ*, **926**, 115
- Jones D. H., et al., 2009, *MNRAS*, **399**, 683
- J zsa G. I. G., et al., 2020, CARACal: Containerized Automated Radio Astronomy Calibration pipeline, Astrophysics Source Code Library, record ascl:2006.014 (ascl:2006.014)
- Karachentsev I. D., Tully R. B., Makarova L. N., Makarov D. I., Rizzi L., 2015, *ApJ*, **805**, 144
- Kenyon J. S., Smirnov O. M., Grobler T. L., Perkins S. J., 2018, *MNRAS*, **478**, 2399
- Kere  D., Katz N., Weinberg D. H., Dav  R., 2005, *MNRAS*, **363**, 2
- Kere  D., Katz N., Fardal M., Dav  R., Weinberg D. H., 2009, *MNRAS*, **395**, 160
- Kraan-Korteweg R. C., Shafi N., Koribalski B. S., Staveley-Smith L., Buckland P., Henning P. A., Fairall A. P., 2008, in *Galaxies in the Local Volume*. p. 13 ([arXiv:0710.1795](https://arxiv.org/abs/0710.1795)), doi:10.1017/S1744501908000000
- Kraljic K., et al., 2018, *MNRAS*, **474**, 547
- Kreckel K., Peebles P. J. E., van Gorkom J. H., van de Weygaert R., van der Hulst J. M., 2011, *AJ*, **141**, 204

- Kreckel K., Platen E., Aragón-Calvo M. A., van Gorkom J. H., van de Weygaert R., van der Hulst J. M., Beygu B., 2012, *AJ*, **144**, 16
- Kurapati S., 2020, PhD thesis, TIFR, National Center for Radio-physics, Pune
- Kurapati S., Chengalur J. N., Pustilnik S., Kamphuis P., 2018, *MNRAS*, **479**, 228
- Kurapati S., Chengalur J. N., Kamphuis P., Pustilnik S., 2020, *MNRAS*, **491**, 4993
- Laigle C., et al., 2018, *MNRAS*, **474**, 5437
- Luber N., van Gorkom J. H., Hess K. M., Pisano D. J., Fernández X., Momjian E., 2019, *AJ*, **157**, 254
- Makhathini S., 2018, PhD thesis, Rhodes University, South Africa
- Meyer M. J., et al., 2004, *MNRAS*, **350**, 1195
- Moorman C. M., Vogeley M. S., Hoyle F., Pan D. C., Haynes M. P., Giovanelli R., 2014, *MNRAS*, **444**, 3559
- Moorman C. M., Vogeley M. S., Hoyle F., Pan D. C., Haynes M. P., Giovanelli R., 2015, *ApJ*, **810**, 108
- Moorman C. M., Moreno J., White A., Vogeley M. S., Hoyle F., Giovanelli R., Haynes M. P., 2016, *ApJ*, **831**, 118
- Paranjape A., Hahn O., Sheth R. K., 2018, *MNRAS*, **476**, 5442
- Park C., Choi Y.-Y., Vogeley M. S., Gott J. Richard I., Blanton M. R., SDSS Collaboration 2007, *ApJ*, **658**, 898
- Parkash V., Brown M. J. I., Jarrett T. H., Bonne N. J., 2018, *ApJ*, **864**, 40
- Patiri S. G., Prada F., Holtzman J., Klypin A., Betancort-Rijo J., 2006, *MNRAS*, **372**, 1710
- Ponomareva A. A., et al., 2021, *MNRAS*, **508**, 1195
- Pujol A., Hoffmann K., Jiménez N., Gaztañaga E., 2017, *A&A*, **598**, A103
- Pustilnik S. A., Tepliakova A. L., 2011, *MNRAS*, **415**, 1188
- Pustilnik S. A., Engels D., Kniazev A. Y., Pramskij A. G., Ugryumov A. V., Hagen H. J., 2006, *Astronomy Letters*, **32**, 228
- Pustilnik S. A., Tepliakova A. L., Makarov D. I., 2019, *MNRAS*, **482**, 4329
- Radburn-Smith D. J., Lucey J. R., Woudt P. A., Kraan-Korteweg R. C., Watson F. G., 2006, *MNRAS*, **369**, 1131
- Ramatsoku M., et al., 2016, *MNRAS*, **460**, 923
- Ricciardelli E., Cava A., Varela J., Quilis V., 2014, *MNRAS*, **445**, 4045
- Rieder S., van de Weygaert R., Cautun M., Beygu B., Portegies Zwart S., 2013, *MNRAS*, **435**, 222
- Rizzi L., Tully R. B., Shaya E. J., Kourkchi E., Karachentsev I. D., 2017, *ApJ*, **835**, 78
- Rojas R. R., Vogeley M. S., Hoyle F., Brinkmann J., 2004, *ApJ*, **617**, 50
- Rojas R. R., Vogeley M. S., Hoyle F., Brinkmann J., 2005, *ApJ*, **624**, 571
- Rosas-Guevara Y., Tissera P., Lagos C. d. P., Paillas E., Padilla N., 2022, *MNRAS*, **517**, 712
- Serra P., et al., 2015, *MNRAS*, **448**, 1922
- Shaya E. J., Tully R. B., Hoffman Y., Pomarède D., 2017, *ApJ*, **850**, 207
- Sheth R. K., van de Weygaert R., 2004, *MNRAS*, **350**, 517
- Stanonik K., Platen E., Aragón-Calvo M. A., van Gorkom J. H., van de Weygaert R., van der Hulst J. M., Peebles P. J. E., 2009, *ApJ*, **696**, L6
- Staveley-Smith L., Kraan-Korteweg R. C., Schröder A. C., Henning P. A., Koribalski B. S., Stewart I. M., Heald G., 2016, *AJ*, **151**, 52
- Szomoru A., van Gorkom J. H., Gregg M. D., Strauss M. A., 1996, *AJ*, **111**, 2150
- Tempel E., Stoica R. S., Martínez V. J., Liivamägi L. J., Castellan G., Saar E., 2014, *MNRAS*, **438**, 3465
- Tully R. B., 1987, *ApJ*, **321**, 280
- Tully R. B., Shaya E. J., Karachentsev I. D., Courtois H. M., Kocevski D. D., Rizzi L., Peel A., 2008, *ApJ*, **676**, 184
- Tully R. B., Pomarède D., Graziani R., Courtois H. M., Hoffman Y., Shaya E. J., 2019, *ApJ*, **880**, 24
- Weinberg D. H., Szomoru A., Guhathakurta P., van Gorkom J. H., 1991, *ApJ*, **372**, L13
- Westmeier T., et al., 2021, *MNRAS*, **506**, 3962
- Wong O. I., et al., 2006, *MNRAS*, **371**, 1855
- Woudt P. A., Kraan-Korteweg R. C., 2001, *A&A*, **380**, 441
- Woudt P. A., Kraan-Korteweg R. C., Cayatte V., Balkowski C., Felenbok P., 2004, *A&A*, **415**, 9
- Zitrin A., Brosch N., 2008, *MNRAS*, **390**, 408
- de Blok W. J. G., Walter F., 2014, *AJ*, **147**, 96
- van de Weygaert R., Platen E., 2011, in International Journal of Modern Physics Conference Series. pp 41–66 ([arXiv:0912.2997](https://arxiv.org/abs/0912.2997)), doi:10.1142/S2010194511000092
- van de Weygaert R., van Kampen E., 1993, *MNRAS*, **263**, 481
- von Benda-Beckmann A. M., Müller V., 2008, *MNRAS*, **384**, 1189

APPENDIX A: LV-SMGPS ATLAS

In this appendix, we present moment maps and spectra for some of the detected galaxies. Figure A1 displays: (i) The integrated HI intensity map. The galaxy ID (Jhhmmss \pm ddmms) for each galaxy is shown on the top-left of moment 0 map. (ii) The intensity-weighted first moment of the galaxy, The synthesis beam FWHM is indicated by an ellipse in both the moment 0 and moment 1 maps. and (iii) The global HI profile of the galaxy is shown by solid black line. The smoothed profile by a black dashed line and the solid red line indicates the heliocentric velocity. The moment maps and spectra for all detected galaxies are available online.

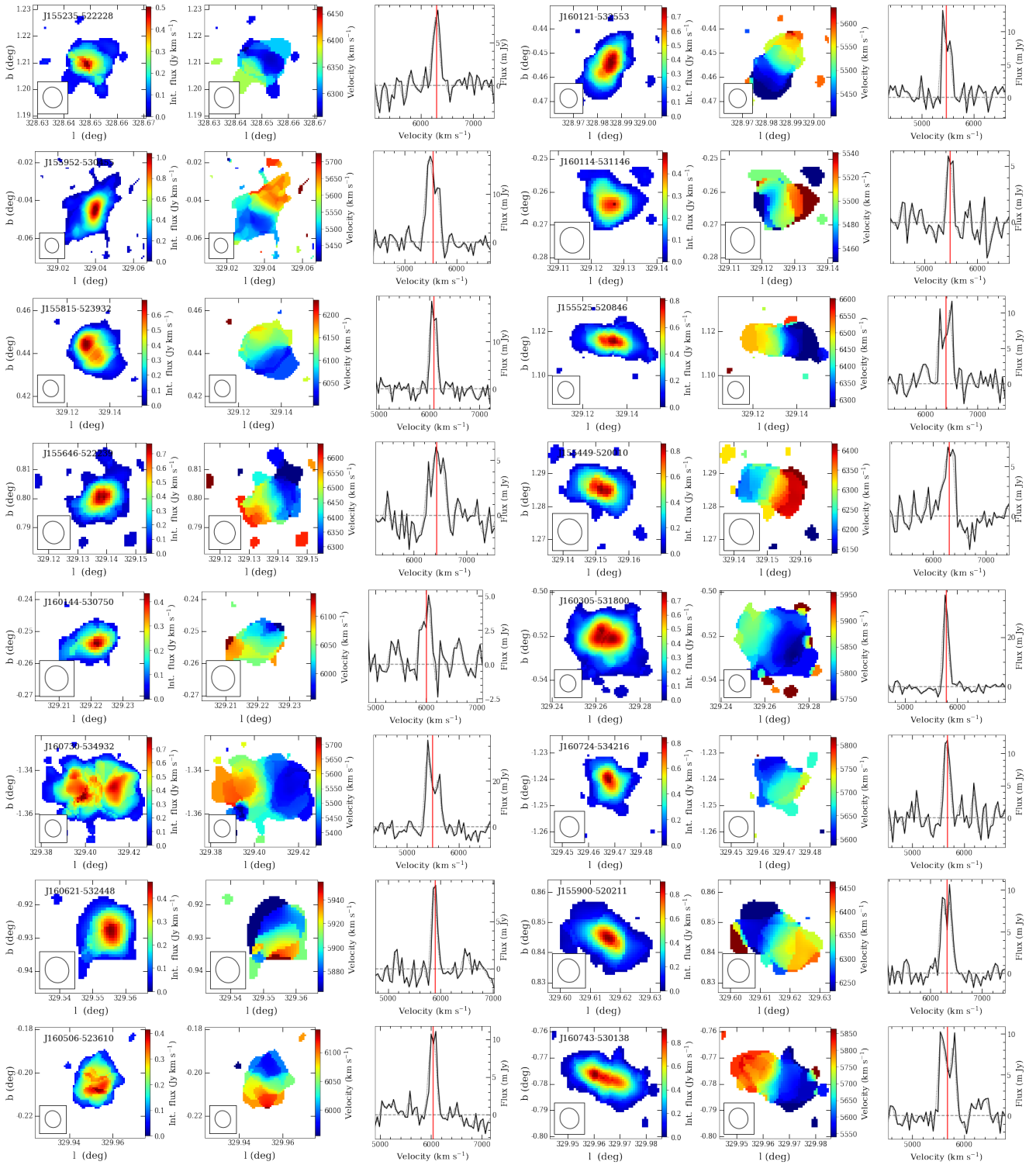


Figure A1. Moment maps and spectra for a few of the detected galaxies are shown in this figure. The moment maps and spectra of all detections are available online.